Optical Materials 123 (2022) 111891

Contents lists available at ScienceDirect

Optical Materials

journal homepage: www.elsevier.com/locate/optmat

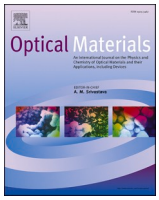

Optimization of a Pb-free all-perovskite tandem solar cell with 30.85% efficiency

Arman U. Duha [a], Mario F. Borunda [a,b,*]

[a] Department of Physics, Oklahoma State University, Stillwater, OK, 74 078, USA
[b] Oklahoma Photovoltaic Research Institute, OK, USA

ARTICLE INFO

Keywords:
Perovskite
Lead-free
Multi-junction
Tandem
SCAPS-1D
High-efficiency

ABSTRACT

We present simulation results obtained with the SCAPS-1D simulation package of a lead-free all-perovskite tandem solar cell. The top and bottom subcells, consisting of $MAGeI_3$, and $FASnI_3$, respectively, were optimized individually by varying material properties such as thickness, electron affinity, and capture cross-section. These standalone optimized subcells are then utilized for the tandem structure. The optimal tandem cell thickness was determined based on short circuit current density (J_{SC}) matching of the standalone subcells by varying the subcells' thickness. A matching J_{SC} of 14.70 mA/cm^2 was obtained for the top and bottom subcell thickness of 983 nm and 1600 nm, respectively. At this current matching condition, the simulation show that a tandem cell would yield a high open-circuit voltage (V_{OC}) of 2.63 V, resulting in an efficiency of 30.85%, significantly higher than that of each subcell.

1. Introduction

In single-junction solar cells, the Shockley-Queisser limit bounds the power conversion efficiency (PCE) to about 33% [1]. That is because a single-junction solar cell does not absorb photons with energies lower than the bandgap, E_g, of the semiconductor absorber. When absorbing photons with energy higher than E_g, the generated electron and hole will each have excess kinetic energy, which is usually relaxed by phonon interactions and thus heating of the lattice [2]. A tandem solar cell minimizes these spectral losses and converts a higher proportion of sunlight into electricity than a single-junction solar cell. Consequently, a tandem solar cell has a higher Shockley-Queisser limit of 45% [3].

A tandem solar cell consists of two or more different solar cells or absorber layers with different E_g. The layer with larger E_g is positioned above the narrow E_g layer such that the top layer absorbs the higher energy photons and the bottom layer absorbs the lower energy photons. Thus, a tandem solar cell utilizes a wider spectral range and produces a higher photocurrent than a single junction solar cell. Increasing the number of subcells further stretches the theoretical PCE limit to 50%, 54%, and 65% corresponding to three, four, and an infinite number of subcells, respectively [3]. The experimental realization of a tandem solar cell goes back as early as 1978 when a device consisting of AlGaAs/GaAs was seen to have a PCE of ~9% [4]. The top performing dual-junction tandem solar cells today are mostly some combination of III-V semiconductors and/or silicon such as, GaInAsP/GaInAs (32.6 ± 1.4%) [5], GaInP/GaAs (32.8 ± 1.4%) [6], and GaAs/Si (32.8 ± 0.5%) [7]. The efficiency values of these tandem devices are well above that of their corresponding single-junction counterpart. Despite these impressive performances, the search for alternative solar cells continues due to the high manufacturing cost and complex fabrication method of the III-V semiconductors [8].

Perovskites are currently some of the most promising absorber materials for use in solar cells. Perovskite solar cells (PSC) have seen a remarkable improvement in PCE of 25.5% for single-junction from 3.8% in only a decade. In addition to providing excellent performance, PSC has the edge over current commercial solar cells in terms of cost since it is manufactured from cheap, naturally abundant precursor materials. The most significant advantage that makes perovskite materials ideal candidates as the top subcell in a tandem device is the suitable bandgap and the ability to tune the bandgap [9]. Further, perovskite materials have efficient radiative recombination and excellent light absorption properties combined with ease of fabrication [10]. Current tandem solar cells have complex fabrication schemes since simple methods to deposit the top subcell are often incompatible with the stability of the bottom subcell. For perovskite, however, a wide choice of simple processing techniques, e.g., spin coating [11,12], vacuum deposition [13–15], and

* Corresponding author. Department of Physics, Oklahoma State University, Stillwater, OK, 74 078, USA.
E-mail address: mario.borunda@okstate.edu (M.F. Borunda).

https://doi.org/10.1016/j.optmat.2021.111891
Received 25 October 2021; Received in revised form 18 November 2021; Accepted 6 December 2021
Available online 17 December 2021

printing techniques [16–18] are available. Their low temperature (~ 100°) crystallization [19] makes it possible to use the fabrication processes mentioned above without harming the bottom subcell. Indeed, this very young technology has already progressed towards devices approaching the efficiency of the top performing tandem cells mentioned before. Perovskite has been used in tandem solar cells as top subcell with Si (perovskite/Si), CIGS (perovskite/CIGS), and even another perovskite (perovskite/perovskite) that have PCE of 29.2%, 24.2%, and 24.2%, respectively [20].

The use of Si as the bottom subcell presents limiting drawbacks to perovskite tandem solar cells. These include an increase in cost and a reduced throughput [21]. Additionally, using a Si subcell would not be flexible. To that end, intense research is performed on all-perovskite (perovskite/perovskite) tandem solar cells [22,23]. In the short span of four years, the PCE of all-perovskite tandem solar cells has risen to 25.6% in a 0.049 cm^2 device (24.2% in 1-cm^2-area devices) [24] from an initial value of 6.6% [25].

So far, the best performing PSC are mostly manufactured from organic lead halide-based materials. The use of Pb, however, poses a major environmental and health threat, as pointed out by many researchers [26–28]. Therefore, one currently researched avenue is the search for Pb-free alternatives. One potential substitute of Pb, and the most extensively explored one, is Sn [29–32]. Currently, most of the highly efficient Sn-based PSCs use $FASnI_3$ perovskite [33–38]. $FASnI_3$ has excellent properties like high charge-carrier mobilities, while progress is being made in overcoming its current shortcomings like low efficiency and poor chemical stability [39–41]. Another element, Ge, which is in the same group as Pb and Sn, is also a potential substitute for Pb. Ge-based perovskites are expected to show similar solid-state properties to their Pb and Sn analogs [42,43] and $MAGeI_3$ has the potential to become an alternative to $MAPbI_3$ [44]. Indeed, theoretical studies show that $MAGeI_3$ possesses remarkable hole and electron conductive behavior and adequate stability compared to that of $MAPbI_3$ [43]. Furthermore, the high bandgap of ~ 1.9 eV that has been found in the experimentally realized $MAGeI_3$, [45,46] makes it a perfect choice for a top subcell in a tandem solar cell.

In this manuscript, we consider $MAGeI_3$ as the top subcell and $FASnI_3$ as the bottom subcell for the simulation of an all-perovskite tandem solar cell using the SCAPS-1D [47] package. First, the bottom subcell was simulated to fit experimental data, followed by detailed optimization on parameters such as the electron affinity, capture cross-section, and thickness. Next, similar optimization was done for the top subcell. The PCEs of the optimized standalone top and bottom subcells were found to be 23.69% and 19.84%, respectively. For the tandem structure, the current matching condition was achieved by varying the thickness of both subcells.

2. Simulation approach

In a multijunction tandem solar cell, the two subcells can be considered as two diodes connected in series. Thus, the same current flows through the subcells, which is the current of the tandem solar cell. The voltage of the tandem cell is the sum of the voltages in the subcells. Since SCAPS-1D does not fully support a multijunction solar cell, the top and bottom subcells were separately simulated. In between the two cells, we introduced a recombination layer of ITO with a thickness of 20 nm. We follow the simulation method [48–53] in which the top subcell is illuminated by standard AM 1.5G 1 sun, and the bottom subcell is illuminated by the spectra filtered by the top subcell, given by,

$$S(\lambda) = S_0(\lambda)\cdot exp\left(\sum_{i=1}^{4} -a_i(\lambda)d_i\right) \quad (1)$$

where $S(\lambda)$ is the filtered spectrum, $S_0(\lambda)$ is the spectrum incident on the top subcell, $a_i(\lambda)$ is the absorption coefficient of the ith material and d_i is the thickness of the ith material. In our case $i = 1, 2, 3$, and 4 corresponds to TiO_2, $MAGeI_3$, Spiro − OMeTAD, and ITO, respectively. Under this condition, the value of the short circuit current (J_{SC}) of the two subcells is matched by varying their thickness to simulate the final tandem cell.

A schematic representation of the tandem structure is also shown in Fig. 1. The absorption coefficient of TiO_2, $MAGeI_3$, Spiro-OMeTAD, and ITO are taken from literature [54–57]. All the basic input values used in the simulation are taken from literature and listed in Table 1.

3. Results and discussion

3.1. Optimization of parameters for each subcell

Experimental data was used to calibrate parameters for the $FASnI_3$ cell. We reproduce the experimental results for formamidinium [40] using the values presented in Table 1. As shown in Table 2, the simulation result mimics the experimental value closely. Here V_{OC} is the open-circuit voltage, J_{SC} is the short circuit current density, FF is the fill factor, and PCE is the power conversion efficiency.

Our approach optimized three parameters: the electron affinity of the transport layers, the cross-section of defects, and the thickness of each of the layers in the device. The band offsets play essential roles in the performance of the solar cells ([64]). The conduction band offset (CBO) is defined as the difference between the electron affinities of the perovskite and the electron transport layer (ETL). The valence band offset (VBO) is defined as the difference between the electron affinities of the hole transport layer (HTL) and the perovskite plus the difference between the bandgaps of the HTL and the perovskite. To investigate the effect of CBO and VBO, we varied the electron affinity of the ETL and the HTL.

It was found that decreasing the electron affinity of TiO_2 from its initial value of 3.9 eV to 3.5 eV improves the PCE from 1.73% to 8.56%, as shown in Fig. 2 (a), since all parameters decrease monotonically as the electron affinity increases. The initial electron affinity of the HTL (the spiro-OMeTAD) of 2.2 eV (PCE of 1.73%) gives the best performance. Increasing the electron affinity will increase the filling factor and the open-circuit voltage while reducing the short circuit current to zero. As shown in Fig. 2, for $FASnI_3$, a CBO of about 0 eV gives optimum performance and as the value of CBO drops, so does the performance. As for the effect of VBO, we see that the optimum performance is in the 0–0.3 eV range. For other VBO values, the efficiency decreases. These

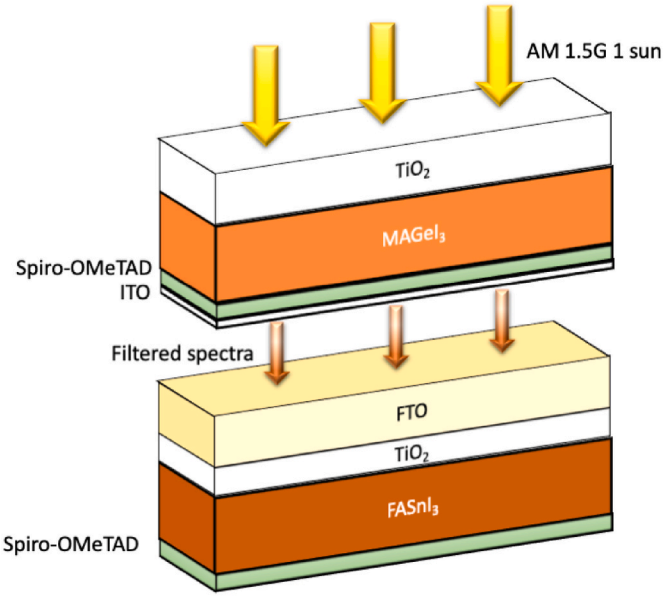

Fig. 1. Schematic device structure of the simulated lead-free halide tandem solar cell.

Table 1
Basic parameters used in the simulation.

Parameters	Spiro-OMeTAD	TiO_2	$MAGeI_3$	$FASnI_3$	FTO
Thickness (nm)	200	350	600	350	400
Bandgap (eV)	3	3.2	1.9	1.41	3.5
Electron affinity (eV)	2.2	3.9	3.98	3.52	4
Dielectric permittivity	3	9[a]	10	8.2	9
Density of states in CB (cm^{-3})	1×10^{19}	1×10^{19}	1×10^{16}	1×10^{18}	2.2×10^{18}
Density of states in VB (cm^{-3})	1×10^{19}	1×10^{19}	1×10^{16}	1×10^{18}	1.8×10^{19}
Thermal velocity of electron (cm/s)	1×10^{7}	1×10^{7}	1×10^{7}	1×10^{7}	1×10^{7}
Thermal velocity of hole (cm/s)	1×10^{7}	1×10^{7}	1×10^{7}	1×10^{7}	1×10^{7}
Electron mobility (cm^2/Vs)	1×10^{-4}	20	162[b]	22	20
Hole mobility (cm^2/Vs)	1×10^{-4}	10	101[b]	22	10
Donor density (cm^{-3})	0	1×10^{17}	1×10^{9}	0	2×10^{19}
Acceptor density (cm^{-3})	2×10^{19}	0	1×10^{9}	7×10^{16}	0
Defect density (cm^{-3})	1×10^{15}	1×10^{15}	1×10^{16}	1×10^{15}	1×10^{15}
References	[58]	[59]; [60]	[61,62]	[63]	[63]

Interface				
Parameters	Spiro/$MAGeI_3$	$MAGeI_3$/TiO_2	Spiro/$FASnI_3$	$FASnI_3$/TiO_2
Defect density (cm^{-3})	1×10^{16}	1×10^{16}	1×10^{16}	1×10^{16}
Capture cross-section (cm^2)	1×10^{-19}	1×10^{-19}	1×10^{-19}	1×10^{-19}
Energetic distribution	Gauss	Gauss	Gauss	Gauss

[a] [60].
[b] [62].

Table 2
Comparison of simulation and experimental results for the $FASnI_3$ cell.

Method	V_{OC} (V)	J_{SC} (mA/cm^2)	FF (%)	PCE (%)
Simulation	0.244	21.09	33.53	1.73
Experimental	0.234	20.45	36.00	1.71

results agree with the literature [63,64].

Defects at the interfaces play a crucial role in the performance of the devices since interface traps are the dominant recombination channel for PSC [65]. Trap-assisted Shockley–Read–Hall (SRH) recombination [66,67] is described by the following expression

$$R_{SRH} = \frac{np - n_i^2}{\tau\left(p + n + 2n_i \cosh\left[\frac{E_i - E_t}{kT}\right]\right)}, \quad \tau = \frac{1}{\sigma N_t v_{th}}, \tag{2}$$

where the electron and hole concentrations are given by n and p, n_i is the instrinsic carriere concentration, τ is the carrier lifetime, N_t and E_t are the defect concentration and defect energy level, v_{th} is the thermal velocity of the carriers, and σ is the carriers capture cross-section. Since the capture cross-section is reported to have a significant effect on the device performance [68], we are interested in calibrating our simulation results to experiment; thus, we investigated the effect of capture cross-section at the ETL/absorber (TiO_2/$FASnI_3$) and the HTL/absorber interface ($FASnI_3$/SpiroOMeTAD).

The results presented in Fig. 3 help us determine the effects on performance from each interface. The ETL/absorber interface shows that decreasing the capture cross-section improves the performance significantly. The PCE increases since all three parameters (FF, J_{SC}, and V_{OC}) increase as the cross-section of trap defects is reduced at the PSC/TiO_2 interface. At the HTL/absorber interface, the open-circuit voltage is constant over a considerable cross-section range and thus limits the maximal PCE.

The thickness of each layer in a solar cell plays an essential role in the device's overall performance. The two competing effects determine the optimal thickness, *viz.*, absorption of incoming photons, and recombination center at the bulk. The absorption of incoming photons increases with increasing thickness per Beer-Lamberts law, $I = I_0 \exp(-\alpha x)$, enhancing the number of photo-generated charge carriers and consequently increasing J_{SC}. However, at the same time, an increase in thickness increases the number of recombination centers, which hinders the charge carriers from contributing to J_{SC}. Thus, it is crucial to find the optimum value of thickness by varying it for each layer.

For a tandem solar cell, the thickness has other especial importance too. Since the top subcell filters the light before it reaches the bottom subcell, minimizing the top subcell thickness is vital for an excellent overall performance. Thickness is also used as the parameter that is varied to obtain the current matching condition.

We explored the effect of thickness of each of the layers on the so far optimized device. In Fig. 4 (a), we see that increasing the thickness of $FASnI_3$ improves PCE until reaching a thickness of about 1400 nm,

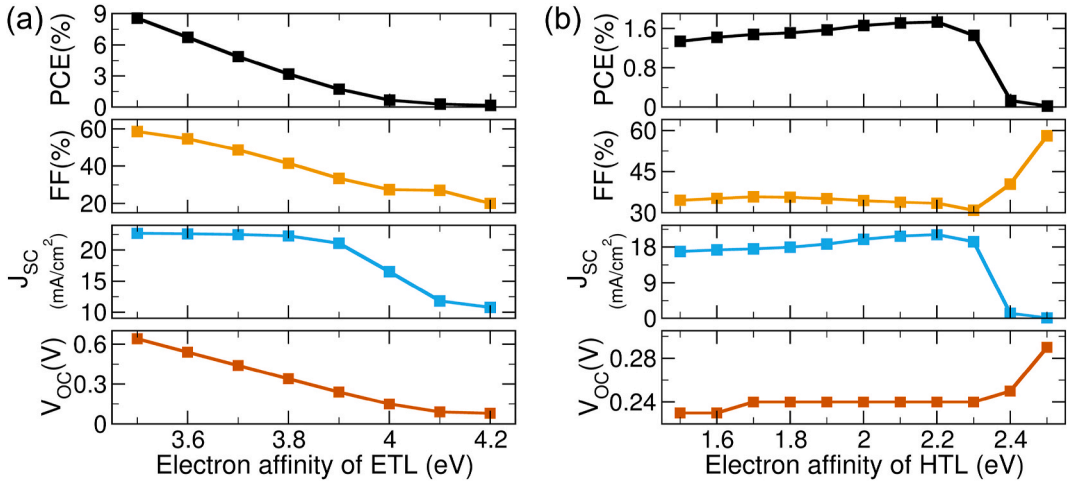

Fig. 2. PCE, FF, J_{SC}, and V_{OC} for the $FASnI_3$ subcell as a function of electron affinity of (a) the electron transport layer and (b) the hole transport layer for the $FASnI_3$ device.

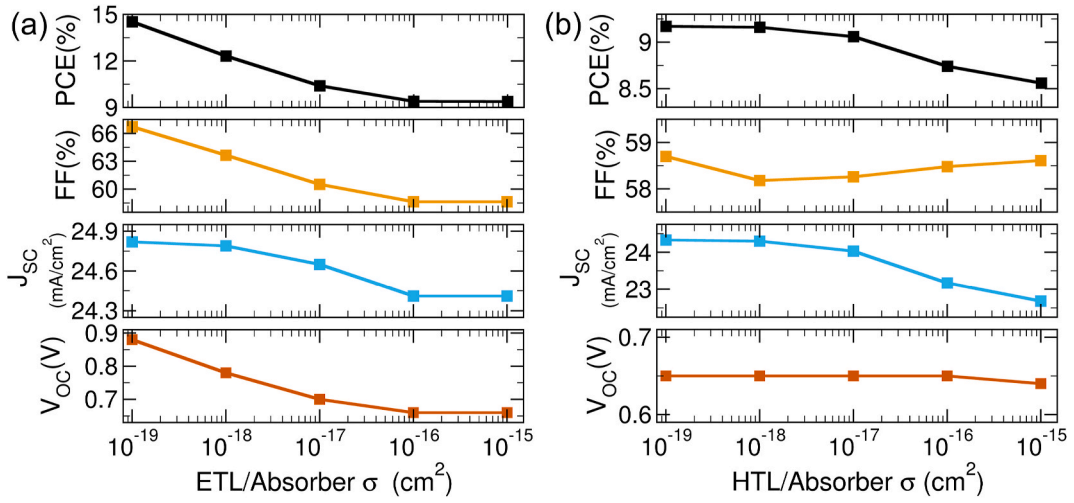

Fig. 3. PCE, FF, J_{SC}, and V_{OC} as a function of capture cross-section at (a) the ETL/absorber interface and (b) the HTL/absorber interface for the $FASnI_3$ absorber.

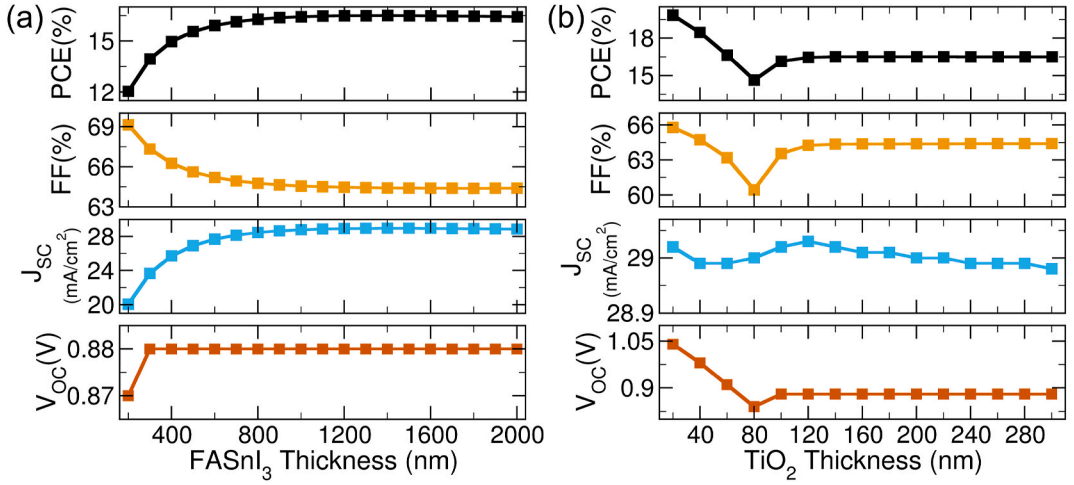

Fig. 4. PCE, FF, J_{SC}, and V_{OC} as a function of (a) absorber thickness and (b) ETL thickness.

where the PCE saturates. The thickness of the HTL has minimal effect on the performance of the device. Our calculations show that the PCE will stay around 16.5%, FF at 64.5%, J_{SC} at 28.97 mA/cm^2, and V_{OC} at 0.88 V over a range of thickness of 20–200 nm. The ETL thickness, however, affects the V_{OC} and the FF, which are more prominent for the thinner films. Thus the PCE of the device is maximal for a 20 nm TiO2 film, as shown in Fig. 4 (b). The final configuration for the optimized $FASnI_3$ subcell and the current-voltage (I–V) characteristics are presented in Table 3.

The $MAGeI_3$ subcell was simulated with the values presented in Table 1. The corresponding J-V curve and the I–V characteristics are shown in Fig. 5. We now present the results of the optimization of the different characteristics of the subcell.

We performed several simulations to find the optimal values of the $MAGeI_3$ subcell. Fig. 6 (a) shows the electron affinity for the ETL. It was found that decreasing electron affinity increases both the J_{SC} and V_{OC}.

Table 3
Device performance for the optimized $FASnI_3$ subcell.

Parameters	Spiro-OMeTAD	TiO_2	$FASnI_3$	HTL/$FASnI_3$	$FASnI_3$/ETL
Electron affinity (eV)	2.2	3.5	3.52	–	–
Capture cross-section (cm^2)	–	–	–	1×10^{-19}	1×10^{-19}
Thickness (nm)	200	20	1400	–	–
I–V characteristics					
V_{OC} (V)	J_{SC} (mA/cm^2)		FF (%)		PCE (%)
1.04	29.02		65.78		19.84

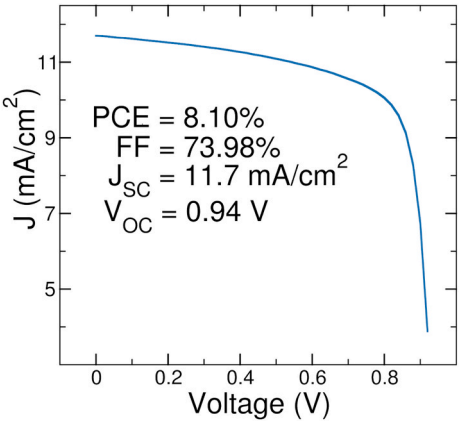

Fig. 5. Simulated J-V curve and I–V characteristic for the initial $MAGeI_3$ subcell.

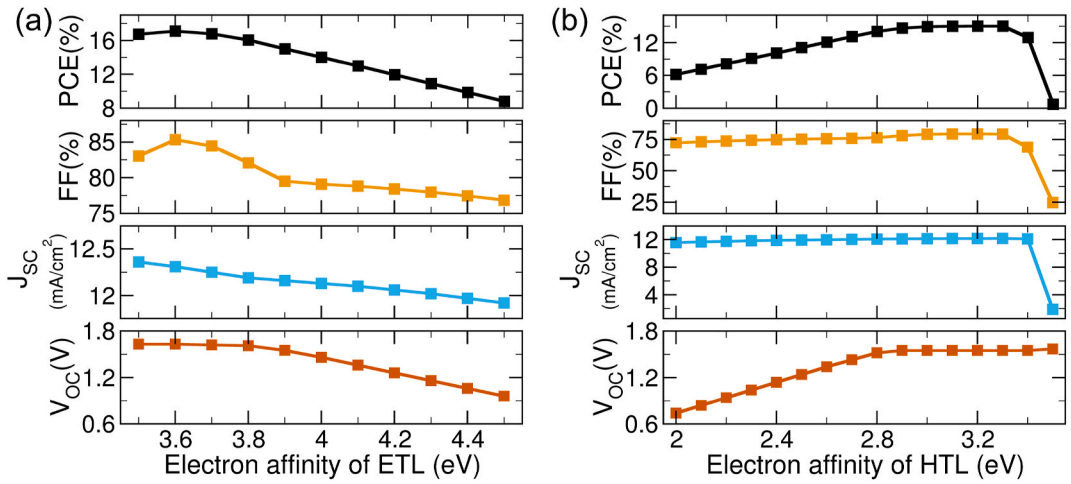

Fig. 6. PCE, FF, J_{SC}, and V_{OC} for the $MAGeI_3$ subcell as a function of electron affinity of (a) the electron transport layer and (b) the hole transport layer for the $MAGeI_3$ device.

However, for the ETL, the maximum filling factor is achieved when the electron affinity is set to 3.6 eV. Thus, the optimal PCE of 17.11% is found for the electron affinity of 3.6 eV. Fig. 6 (b) shows the electron affinity for the HTL. We found that the V_{OC} increases linearly with electron affinity until saturating at a value of 1.55 V once the affinity reaches around 2.9 eV. The J_{SC} increases as the electron affinity increases slowly until reaching a value of 12.17 mA/cm^2 at an affinity of 3.3 eV, afterward, it declines. Similarly, the filling factor presents a slowly increasing trend with an increase of electron affinity. The maximum FF is 79.51% at an electron affinity of 3.2 eV. The PCE has a maximum value of 15.01% when the electron affinity of the HTL is set to 3.2 eV.

Using this optimized electron affinity value, we examined the effect of capture cross-section at the interfaces. The results shown in Fig. 7 show that capture cross-section does not have as much impact on the performance of $MAGeI_3$ as it does in the $FASnI_3$. At the ETL/absorber interface, decreasing the capture cross-section improves the performance since all three parameters (FF, J_{SC}, and V_{OC}) increase as the cross-section of the trap defects is reduced. At the HTL/absorber interface, the three parameters stay constant over the cross-section range considered with a minimal increase as the cross-section is reduced and thus the 17.21% PCE. From these values, the capture cross-section used for the rest of the simulations of $MAGeI_3$ were kept unchanged.

Finally, the thicknesses of all the layers were varied. As seen from Fig. 8 (a), the PCE improves with increasing thickness of $MAGeI_3$. The rate of increase as the film thickness increases is not saturating as it was in the FA-based cell until reaching a thickness of 2000 nm. We have chosen 2000 nm as the thickness of $MAGeI_3$. The thickness of the HTL has minimal effect on the overall performance of the device. For the HTL layer, our calculations show that the PCE will stay around 23.24%, FF around 83.6%, J_{SC} at 17.55 mA/cm^2, and V_{OC} at 1.58 V over a range of thickness from 20 to 200 nm. There is a decrease for all three parameters as the thickness of the ETL increases and, since the top subcell should be as thin as possible so that more light can reach the bottom cell, we choose 20 nm for HTL and ETL. The final configuration for the optimized $MAGeI_3$ subcell and the I–V characteristics is summarized in Table 4.

3.2. Tandem solar cell simulation

In simulating the tandem solar cell, the bottom subcell is illuminated by the light filtered by the top subcell. The filtered light is calculated using Eqn. (1) and thus, the current matching condition (the top and bottom subcell having the same J_{SC}) is satisfied. We note that a thinning of the top subcell is required to match the J_{SC} of the bottom subcell. To find the right combination of thickness, filtered spectra $S(\lambda)$ for several different thicknesses of the top subcell are calculated. The thickness of the bottom cell is also varied for each spectrum. Fig. 9 presents the simulated J_{SC} of the top subcell (black line) as a function of thickness

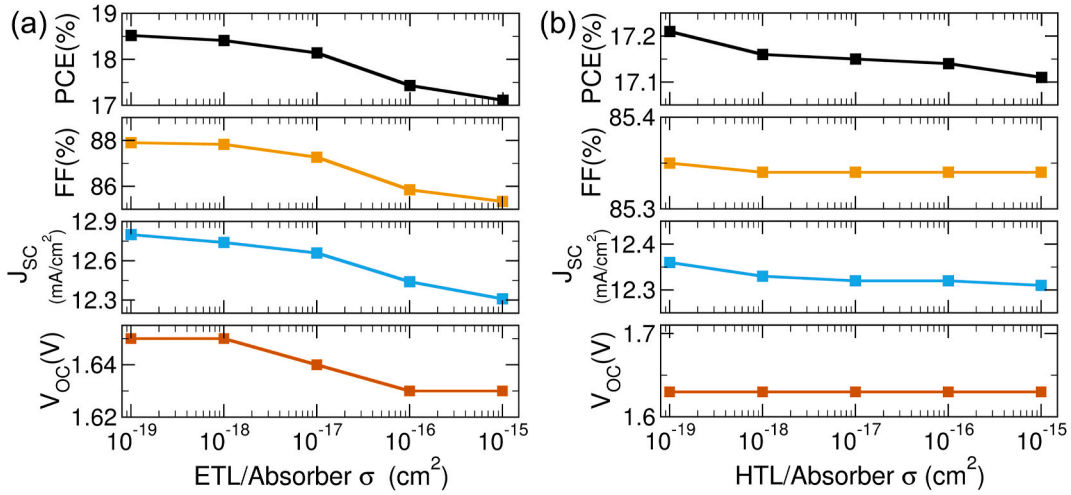

Fig. 7. PCE, FF, J_{SC}, and V_{OC} as a function of capture cross-section at (a) the ETL/absorber interface and (b) the HTL/absorber interface for the $MAGeI_3$ absorber.

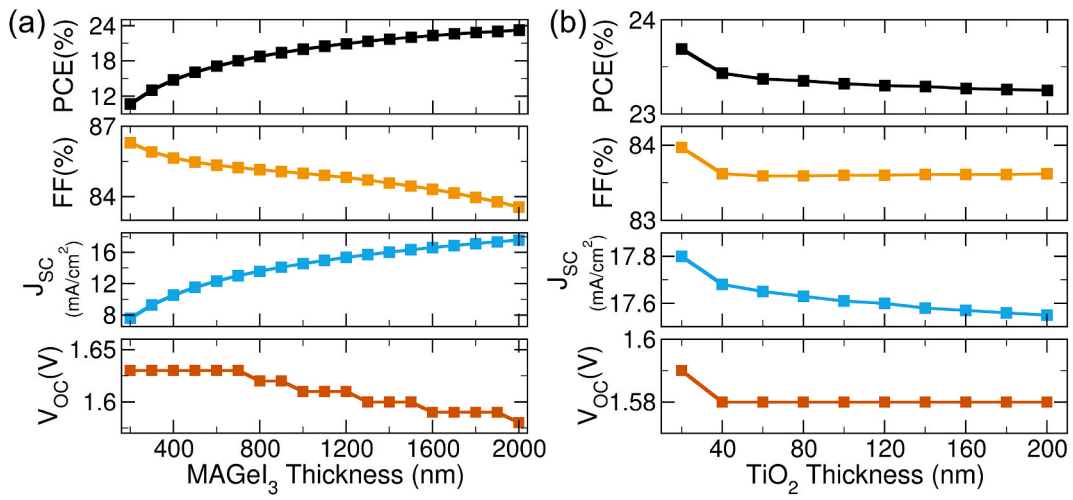

Fig. 8. PCE, FF, J_{SC}, and V_{OC} as a function of (a) absorber thickness and (b) ETL thickness.

Table 4
Optimized $MAGeI_3$ subcell.

Parameters	Spiro-OMeTAD	TiO_2	$MAGeI_3$	HTL/$MAGeI_3$	$MAGeI_3$/ETL
Electron affinity (eV)	3.2	3.6	3.98	–	–
Capture cross-section (cm^2)	–	–	–	1×10^{-15}	1×10^{-15}
Thickness (nm)	20	20	2000	–	–
I–V characteristics					
V_{OC} (V)	J_{SC} (mA/cm^2)		FF (%)		PCE (%)
1.59	17.80		83.97		23.69

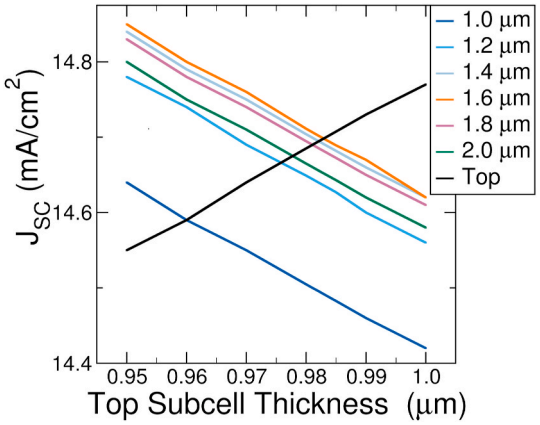

Fig. 9. Simulated J_{SC} of the top subcell (black line) as a function of thickness and the J_{SC} of the bottom subcell for several thicknesses (color lines). The matching condition requires that equal short circuit current flows in the device thus for each thickness of the bottom subcell there is one particular thickness of the top subcell.

along with the short-circuit current of the bottom subcell for several thicknesses (color lines). The best current matching condition is obtained with a top subcell thickness of 983 nm and bottom subcell thickness of 1600 nm, both having $J_{SC} = 14.70$ mA/cm^2. The J-V curve for this configuration and those of the individual subcells are shown in Fig. 10. The I–V characteristics are presented in Table 5.

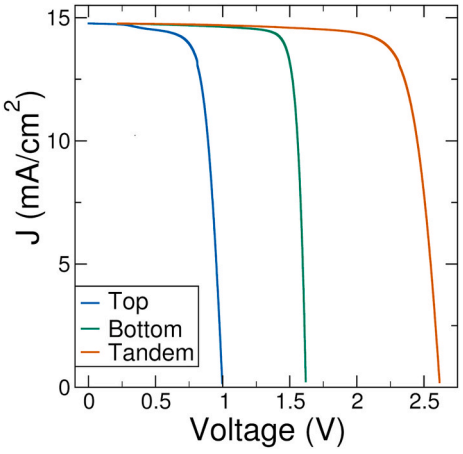

Fig. 10. Simulated J-V curve of the individual top subcell, the bottom subcell, and the tandem cell under the current matching condition.

Table 5
I–V characteristics of the individual subcells and the tandem cell.

Cell	V_{OC} (V)	J_{SC} (mA/cm^2)	FF (%)	PCE (%)
Top subcell	1.62	14.70	85.44	20.31
Bottom subcell	1.01	14.70	71.68	17.10
tandem	2.63	14.70	79.80	30.85

4. Conclusion

In this study, the numerical simulation of a monolithic 2-terminal all-perovskite tandem solar cell has been analyzed. The electron affinity of the electron and hole transport layers, the cross-section of defects, and the thickness of each component were varied using the SCAPS-1D solar cell simulator to understand their effect on the PCE. The simulation of the tandem device was done with the bottom subcell being illuminated with the light filtered by the top subcell, thus ensuring a realistic analysis. Given the current matching condition, our simulation results showed that the J_{SC} of the tandem device is limited by the J_{SC} of the bottom subcell. Thinning of the top subcell is necessary to match the current across the device. While the J_{SC} of the tandem device is smaller than the currents of the optimized individual subcells, a high V_{OC} of 2.63 V in the tandem device results in a significantly higher PCE of 30.85% compared to that of individual subcells.

The optimal thickness of the subcells found was 1.6 μm and 983 nm. The calculated PCE for those thicknesses will be higher than experimental values, given that the calculations consider only the dominant scattering channel, trap defects at the interface, and ignore scattering at grain boundaries. However, if we reduce the thickness of both cells to be below 1 μm, we still see a large PCE. For instance, when the thickness of the $FASnI_3$ is set to 1 μm, the current matching condition requires the layer $MAGeI_3$ to be 961 nm and the results we obtain are that the J_{SC} is 14.6 mA/cm^2, V_{OC} is 2.63 V, FF is 80%, and PCE is reduced from the optimal 30.85% to 30.73%. Overall, these results suggest that lead-free perovskites can compete with lead-based devices in all-perovskite tandem solar cells. Further improvement in the performance of the tandem device can be achieved by utilizing a bottom subcell that can provide higher J_{SC}.

CRediT authorship contribution statement

Arman U. Duha: Conceptualization, Methodology, Software, Validation, Formal analysis, Investigation, Data curation, Writing – original draft, Writing – review & editing, Visualization. **Mario F. Borunda:** Conceptualization, Validation, Data curation, Writing – original draft, Writing – review & editing, Visualization, Project administration, Funding acquisition, Supervision.

Declaration of competing interest

The authors declare that they have no known competing financial interests or personal relationships that could have appeared to influence the work reported in this paper.

Acknowledgements

The authors are thankful to the funding support of the National Aeronautics and Space Administration under Agreement No. 80NSSC19M0140 issued through NASA Oklahoma EPSCoR. The authors also thank Dr. Andrew Yost, Dr. Bayram Saparov, Dr. Do Young Kim and Md. Tohidul Islam for stimulating discussions.

References

[1] W. Shockley, H.J. Queisser, Detailed balance limit of efficiency of p-n junction solar cells, J. Appl. Phys. 32 (3) (1961) 510–519.
[2] L.C. Hirst, N.J. Ekins-Daukes, Fundamental losses in solar cells, Prog. Photovolt. 19 (3) (2011) 286–293.
[3] A. Marti, G.L. Araújo, Limiting efficiencies for photovoltaic energy conversion in multigap systems, Sol. Energy Mater. Sol. Cells 43 (2) (1996) 203–222.
[4] S. Bedair, M. Lamorte, J. Hauser, A two-junction cascade solar-cell structure, Appl. Phys. Lett. 34 (1) (1979) 38–39.
[5] N. Jain, K.L. Schulte, J.F. Geisz, D.J. Friedman, R.M. France, E.E. Perl, A. G. Norman, H.L. Guthrey, M.A. Steiner, High-efficiency inverted metamorphic 1.7/1.1 eV GaInAsP/GaInAs dual-junction solar cells, Appl. Phys. Lett. 112 (5) (2018), 053905.
[6] M. Green, E. Dunlop, J. Hohl-Ebinger, M. Yoshita, N. Kopidakis, X. Hao, Solar cell efficiency tables (version 57), Prog. Photovolt. 29 (1) (2021) 3–15.
[7] S. Essig, C. Allebé, T. Remo, J.F. Geisz, M.A. Steiner, K. Horowitz, L. Barraud, J. S. Ward, M. Schnabel, A. Descoeudres, et al., Raising the one-sun conversion efficiency of III–V/Si solar cells to 32.8% for two junctions and 35.9% for three junctions, Nat. Energy 2 (9) (2017) 1–9.
[8] P.A. Basore, Economics of tandem flat plate photovoltaic modules, in: 2016 IEEE 43rd Photovoltaic Specialists Conference (PVSC), IEEE, 2016, pp. 2635–2637.
[9] G.E. Eperon, S.D. Stranks, C. Menelaou, M.B. Johnston, L.M. Herz, H.J. Snaith, Formamidinium lead trihalide: a broadly tunable perovskite for efficient planar heterojunction solar cells, Energy Environ. Sci. 7 (3) (2014) 982–988.
[10] N.N. Lal, Y. Dkhissi, W. Li, Q. Hou, Y.-B. Cheng, U. Bach, Perovskite tandem solar cells, Adv. Energy Mater. 7 (18) (2017) 1602761.
[11] N.J. Jeon, J.H. Noh, Y.C. Kim, W.S. Yang, S. Ryu, S.I. Seok, Solvent engineering for high-performance inorganic–organic hybrid perovskite solar cells, Nat. Mater. 13 (9) (2014) 897–903.
[12] M. Saliba, T. Matsui, J.-Y. Seo, K. Domanski, J.-P. Correa-Baena, M.K. Nazeeruddin, S.M. Zakeeruddin, W. Tress, A. Abate, A. Hagfeldt, et al., Cesium-containing triple cation perovskite solar cells: improved stability, reproducibility and high efficiency, Energy Environ. Sci. 9 (6) (2016) 1989–1997.
[13] J. Ávila, C. Momblona, P. Boix, M. Sessolo, M. Anaya, G. Lozano, K. Vandewal, H. Míguez, H.J. Bolink, High voltage vacuum-deposited $CH_3NH_3PbI_3$–$CH_3NH_3PbI_3$ tandem solar cells, Energy Environ. Sci. 11 (11) (2018) 3292–3297.
[14] J. Borchert, R.L. Milot, J.B. Patel, C.L. Davies, A.D. Wright, L. Martinez Maestro, H. J. Snaith, L.M. Herz, M.B. Johnston, Large-area, highly uniform evaporated formamidinium lead triiodide thin films for solar cells, ACS Energy Lett. 2 (12) (2017) 2799–2804.
[15] C. Momblona, L. Gil-Escrig, E. Bandiello, E.M. Hutter, M. Sessolo, K. Lederer, J. Blochwitz-Nimoth, H.J. Bolink, Efficient vacuum deposited p–i–n and n–i–p perovskite solar cells employing doped charge transport layers, Energy Environ. Sci. 9 (11) (2016) 3456–3463.
[16] T. Abzieher, S. Moghadamzadeh, F. Schackmar, H. Eggers, F. Sutterluti, A. Farooq, D. Kojda, K. Habicht, R. Schmager, A. Mertens, et al., Electron-beam-evaporated nickel oxide hole transport layers for perovskite-based photovoltaics, Adv. Energy Mater. 9 (12) (2019) 1802995.
[17] C. Ilie, F. Guzman, B. Swanson, I. Evans, P. Costa, J. Teeter, M. Shekhirev, N. Benker, S. Sikich, A. Enders, et al., Inkjet printable-photoactive all inorganic perovskite films with long effective photocarrier lifetimes, J. Phys. Condens. Matter 30 (18) (2018) 18LT02.
[18] F. Mathies, H. Eggers, B.S. Richards, G. Hernandez-Sosa, U. Lemmer, U. W. Paetzold, Inkjet-printed triple cation perovskite solar cells, ACS Appl. Energy Mater. 1 (5) (2018) 1834–1839.
[19] M. Jošt, L. Kegelmann, L. Korte, S. Albrecht, Monolithic perovskite tandem solar cells: a review of the present status and advanced characterization methods toward 30% efficiency, Adv. Energy Mater. 10 (26) (2020) 1904102.
[20] B. Ehrler, E. Alarcón-Lladó, S.W. Tabernig, T. Veeken, E.C. Garnett, A. Polman, Photovoltaics reaching for the Shockley–Queisser limit, ACS Energy Lett. 5 (2020) 3029–3033, 9th ACS.
[21] A.F. Palmstrom, G.E. Eperon, T. Leijtens, R. Prasanna, S.N. Habisreutinger, W. Nemeth, E.A. Gaulding, S.P. Dunfield, M. Reese, S. Nanayakkara, T. Moot, J. Werner, J. Liu, B. To, S.T. Christensen, M.D. McGehee, M.F. van Hest, J. M. Luther, J.J. Berry, D.T. Moore, Enabling flexible all-perovskite tandem solar cells, Joule 3 (9) (2019) 2193–2204. URL, https://www.sciencedirect.com/science/article/pii/S2542435119302521.
[22] R. He, S. Ren, C. Chen, Z. Yi, Y. Luo, H. Lai, W. Wang, G. Zeng, X. Hao, Y. Wang, et al., Wide-bandgap organic-inorganic hybrid and all-inorganic perovskite solar cells and their application in all-perovskite tandem solar cells, Energy Environ. Sci. 14 (2021) 5723–5759, https://doi.org/10.1039/D1EE01562A.
[23] D. Zhao, L. Ding, All-perovskite tandem structures shed light on thin-film photovoltaics, Sci. Bull. 65 (14) (2020) 1144–1146. https://www.sciencedirect.com/science/article/pii/S2095927320302243.
[24] K. Xiao, R. Lin, Q. Han, Y. Hou, Z. Qin, H.T. Nguyen, J. Wen, M. Wei, V. Yeddu, M. I. Saidaminov, et al., All-perovskite tandem solar cells with 24.2% certified efficiency and area over 1 cm^2 using surface-anchoring zwitterionic antioxidant, Nat. Energy 5 (11) (2020) 870–880.
[25] F. Jiang, T. Liu, B. Luo, J. Tong, F. Qin, S. Xiong, Z. Li, Y. Zhou, A two-terminal perovskite/perovskite tandem solar cell, J. Mater. Chem. A 4 (4) (2016) 1208–1213.
[26] A. Babayigit, A. Ethirajan, M. Muller, B. Conings, Toxicity of organometal halide perovskite solar cells, Nat. Mater. 15 (3) (2016) 247–251.
[27] A. Babayigit, D.D. Thanh, A. Ethirajan, J. Manca, M. Muller, H.-G. Boyen, B. Conings, Assessing the toxicity of Pb-and Sn-based perovskite solar cells in model organism Danio rerio, Sci. Rep. 6 (1) (2016) 1–11.
[28] L. Serrano-Lujan, N. Espinosa, T.T. Larsen-Olsen, J. Abad, A. Urbina, F.C. Krebs, Tin-and lead-based perovskite solar cells under scrutiny: an environmental perspective, Adv. Energy Mater. 5 (20) (2015) 1501119.
[29] X. Jiang, H. Li, Q. Zhou, Q. Wei, M. Wei, L. Jiang, Z. Wang, Z. Peng, F. Wang, Z. Zang, et al., One-step synthesis of SnI_2(DMSO) adducts for high-performance tin perovskite solar cells, J. Am. Chem. Soc. 143 (29) (2021) 10970–10976.
[30] X. Jiang, F. Wang, Q. Wei, H. Li, Y. Shang, W. Zhou, C. Wang, P. Cheng, Q. Chen, L. Chen, Z. Ning, Ultra-high open-circuit voltage of tin perovskite solar cells via an electron transporting layer design, Nat. Commun. 11 (1) (2020) 1245.
[31] Z. Wan, H. Lai, S. Ren, R. He, Y. Jiang, J. Luo, Q. Chen, X. Hao, Y. Wang, J. Zhang, L. Wu, D. Zhao, Interfacial engineering in lead-free tin-based perovskite solar cells, J. Energy Chem. 57 (2021) 147–168. URL, https://www.sciencedirect.com/science/article/pii/S2095495620306161.
[32] S. Yang, W. Fu, Z. Zhang, H. Chen, C.-Z. Li, Recent advances in perovskite solar cells: efficiency, stability and lead-free perovskite, J. Mater. Chem. A 5 (23) (2017) 11462–11482.
[33] F. Gu, S. Ye, Z. Zhao, H. Rao, Z. Liu, Z. Bian, C. Huang, Improving performance of lead-free formamidinium tin triiodide perovskite solar cells by tin source purification, Solar RRL 2 (10) (2018) 1800136.
[34] E. Jokar, C.-H. Chien, C.-M. Tsai, A. Fathi, E.W.-G. Diau, Robust tin-based perovskite solar cells with hybrid organic cations to attain efficiency approaching 10%, Adv. Mater. 31 (2) (2019) 1804835.
[35] W. Ke, C.C. Stoumpos, M. Zhu, L. Mao, I. Spanopoulos, J. Liu, O.Y. Kontsevoi, M. Chen, D. Sarma, Y. Zhang, et al., Enhanced photovoltaic performance and stability with a new type of hollow 3D perovskite {en}$FASnI_3$, Sci. Adv. 3 (8) (2017), e1701293.
[36] S. Shao, J. Liu, G. Portale, H.-H. Fang, G.R. Blake, G.H. ten Brink, L.J.A. Koster, M. A. Loi, Highly reproducible sn-based hybrid perovskite solar cells with 9% efficiency, Adv. Energy Mater. 8 (4) (2018) 1702019.
[37] F. Wang, X. Jiang, H. Chen, Y. Shang, H. Liu, J. Wei, W. Zhou, H. He, W. Liu, Z. Ning, 2D-quasi-2D-3D hierarchy structure for tin perovskite solar cells with enhanced efficiency and stability, Joule 2 (12) (2018) 2732–2743.

[38] B.-B. Yu, Z. Chen, Y. Zhu, Y. Wang, B. Han, G. Chen, X. Zhang, Z. Du, Z. He, Heterogeneous 2D/3D tin-halides perovskite solar cells with certified conversion efficiency breaking 14%, Adv. Mater. 33 (36) (2021) 2102055.
[39] E. Jokar, C.-H. Chien, A. Fathi, M. Rameez, Y.-H. Chang, E.W.-G. Diau, Slow surface passivation and crystal relaxation with additives to improve device performance and durability for tin-based perovskite solar cells, Energy Environ. Sci. 11 (9) (2018) 2353–2362.
[40] T.M. Koh, T. Krishnamoorthy, N. Yantara, C. Shi, W.L. Leong, P.P. Boix, A. C. Grimsdale, S.G. Mhaisalkar, N. Mathews, Formamidinium tin-based perovskite with low E_g for photovoltaic applications, J. Mater. Chem. A 3 (29) (2015) 14996–15000.
[41] X. Meng, J. Lin, X. Liu, X. He, Y. Wang, T. Noda, T. Wu, X. Yang, L. Han, Highly stable and efficient $FASnI_3$-based perovskite solar cells by introducing hydrogen bonding, Adv. Mater. 31 (42) (2019) 1903721.
[42] S.J. Clark, J.D. Donaldson, J.A. Harvey, Evidence for the direct population of solid-state bands by non-bonding electron pairs in compounds of the type $CsMX_3$(M= Ge, Sn, Pb; X = Cl, Br, I), J. Mater. Chem. 5 (1995) 1813–1818.
[43] P.-P. Sun, Q.-S. Li, L.-N. Yang, Z.-S. Li, Theoretical insights into a potential lead-free hybrid perovskite: substituting Pb^{2+} with Ge^{2+}, Nanoscale 8 (3) (2016) 1503–1512.
[44] H. Hu, B. Dong, W. Zhang, Low-toxic metal halide perovskites: opportunities and future challenges, J. Mater. Chem. A 5 (23) (2017) 11436–11449.
[45] T. Krishnamoorthy, H. Ding, C. Yan, W.L. Leong, T. Baikie, Z. Zhang, M. Sherburne, S. Li, M. Asta, N. Mathews, et al., Lead-free germanium iodide perovskite materials for photovoltaic applications, J. Mater. Chem. A 3 (47) (2015) 23829–23832.
[46] C.C. Stoumpos, L. Frazer, D.J. Clark, Y.S. Kim, S.H. Rhim, A.J. Freeman, J. B. Ketterson, J.I. Jang, M.G. Kanatzidis, Hybrid germanium iodide perovskite semiconductors: active lone pairs, structural distortions, direct and indirect energy gaps, and strong nonlinear optical properties, J. Am. Chem. Soc. 137 (21) (2015) 6804–6819.
[47] M. Burgelman, P. Nollet, S. Degrave, Modelling polycrystalline semiconductor solar cells, Thin Solid Films 361 (2000) 527–532.
[48] G.K. Gupta, A. Dixit, Theoretical studies of single and tandem $Cu_2ZnSn\ (S/Se)_4$ junction solar cells for enhanced efficiency, Opt. Mater. 82 (2018) 11–20.
[49] M.T. Islam, M.R. Jani, A.F. Islam, K.M. Shorowordi, S. Chowdhury, S.S. Nishat, S. Ahmed, Investigation of $CsSn_{0.5}Ge_{0.5}I_3$-on-Si tandem solar device utilizing SCAPS simulation, IEEE Trans. Electron. Dev. 68 (2) (2021) 618–625.
[50] M.T. Islam, M.R. Jani, S. Rahman, K.M. Shorowordi, S.S. Nishat, D. Hodges, S. Banerjee, H. Efstathiadis, J. Carbonara, S. Ahmed, Investigation of non-Pb all-perovskite 4-T mechanically stacked and 2-T monolithic tandem solar devices utilizing SCAPS simulation, SN Appl. Sci. 3 (4) (2021) 1–12.
[51] K. Kim, J. Gwak, S.K. Ahn, Y.-J. Eo, J.H. Park, J.-S. Cho, M.G. Kang, H.-E. Song, J. H. Yun, Simulations of chalcopyrite/c-Si tandem cells using SCAPS-1D, Sol. Energy 145 (2017) 52–58.
[52] L. Liu, P. Liu, S. Ullah, S.-E. Yang, H. Guo, L. Wang, X. Wang, Y. Chen, The optimization of $CsPbIBr_2$ top sub-cells for the application in monolithic all-perovskite tandem solar cells, Sol. Energy 228 (2021) 274–281. https://www.sciencedirect.com/science/article/pii/S0038092X21006782.
[53] J. Madan, R. Pandey, R. Sharma, et al., Device simulation of 17.3% efficient lead-free all-perovskite tandem solar cell, Sol. Energy 197 (2020) 212–221.
[54] J. Cui, T. Allen, Y. Wan, J. Mckeon, C. Samundsett, D. Yan, X. Zhang, Y. Cui, Y. Chen, P. Verlinden, et al., Titanium oxide: a re-emerging optical and passivating material for silicon solar cells, Sol. Energy Mater. Sol. Cells 158 (2016) 115–121.
[55] M. Filipič, P. Löper, B. Niesen, S. De Wolf, J. Krč, C. Ballif, M. Topič, $CH_3NH_3PbI_3$ perovskite/silicon tandem solar cells: characterization based optical simulations, Opt. Express 23 (7) (2015) A263–A278.
[56] Z.C. Holman, M. Filipič, A. Descoeudres, S. De Wolf, F. Smole, M. Topič, C. Ballif, Infrared light management in high-efficiency silicon heterojunction and rear-passivated solar cells, J. Appl. Phys. 113 (1) (2013), 013107, https://doi.org/10.1063/1.4772975. URL.
[57] R. Sa, W. Zha, R. Yuan, J. Chen, Exploring electronic and optical properties of Ge-based perovskites under strain: insights from the first-principles calculations, Spectrochim. Acta A Mol. 229 (2020) 118013.
[58] I.M. De Los Santos, H.J. Cortina-Marrero, M. Ruíz-Sánchez, L. Hechavarría-Difur, F. Sánchez-Rodríguez, M. Courel, H. Hu, Optimization of $CH_3NH_3PbI_3$ perovskite solar cells: a theoretical and experimental study, Sol. Energy 199 (2020) 198–205.
[59] A.-A. Kanoun, M.B. Kanoun, A.E. Merad, S. Goumri-Said, Toward development of high-performance perovskite solar cells based on $CH_3NH_3GeI_3$ using computational approach, Sol. Energy 182 (2019) 237–244.
[60] M.D. Stamate, On the dielectric properties of dc magnetron TiO_2 thin films, Appl. Surf. Sci. 218 (1–4) (2003) 318–323.
[61] N. Singh, A. Agarwal, M. Agarwal, Numerical simulation of highly efficient lead-free all-perovskite tandem solar cell, Sol. Energy 208 (2020) 399–410.
[62] Y.-Q. Zhao, B. Liu, Z.-L. Yu, J. Ma, Q. Wan, P.-b. He, M.-Q. Cai, Strong ferroelectric polarization of $CH_3NH_3GeI_3$ with high-absorption and mobility transport anisotropy: theoretical study, J. Mater. Chem. C 5 (22) (2017) 5356–5364.
[63] S. Abdelaziz, A. Zekry, A. Shaker, M. Abouelatta, Investigating the performance of formamidinium tin-based perovskite solar cell by SCAPS device simulation, Opt. Mater. 101 (2020) 109738.
[64] T. Minemoto, M. Murata, Theoretical analysis on effect of band offsets in perovskite solar cells, Sol. Energy Mater. Sol. Cells 133 (2015) 8–14. URL, https://www.sciencedirect.com/science/article/pii/S0927024814005674.
[65] T.S. Sherkar, C. Momblona, L. Gil-Escrig, J. Ávila, M. Sessolo, H.J. Bolink, L.J. A. Koster, Recombination in perovskite solar cells: significance of grain boundaries, interface traps, and defect ions, ACS Energy Lett. 2 (5) (2017) 1214–1222.
[66] R.N. Hall, Electron-hole recombination in germanium, Phys. Rev. 87 (Jul 1952), 387–387. URL, https://link.aps.org/doi/10.1103/PhysRev.87.387.
[67] W. Shockley, W.T. Read, Statistics of the recombinations of holes and electrons, Phys. Rev. 87 (Sep 1952) 835–842. URL, https://link.aps.org/doi/10.1103/PhysRev.87.835.
[68] M. Kumar, A. Raj, A. Kumar, A. Anshul, An optimized lead-free formamidinium Sn-based perovskite solar cell design for high power conversion efficiency by SCAPS simulation, Opt. Mater. 108 (2020) 110213. URL, https://www.sciencedirect.com/science/article/pii/S0925346720305565.